crystals

MDPI

Article

Structural, Morphological and Dielectric Characterization of $BiFeO_3$ Fibers Grown by the LFZ Technique

Marina Vieira Peixoto [1], Florinda Mendes Costa [1], Susana Devesa [1,2,*] and Manuel Pedro Fernandes Graça [1,*]

[1] I3N-Physics Department, University of Aveiro, Campus Universitário de Santiago, 3810-193 Aveiro, Portugal; marinavieirapeixoto@gmail.com (M.V.P.); flor@ua.pt (F.M.C.)
[2] CEMMPRE, Centre for Mechanical Engineering, Materials and Processes, Department of Mechanical Engineering, University of Coimbra, Rua Luís Reis Santos, 3030-788 Coimbra, Portugal
* Correspondence: susana_devesa@hotmail.com (S.D.); mpfg@ua.pt (M.P.F.G.)

Abstract: $BiFeO_3$ fibers were prepared by the Laser Floating Zone (LFZ) technique using different growth speeds. The structural characterization of the samples was undertaken using X-ray diffraction (XRD) and Raman spectroscopy, the morphological characterization by scanning electron microscopy (SEM), and the electrical characterization by impedance spectroscopy. The XRD patterns showed that $BiFeO_3$ was the major phase in all the samples. Fibers grown at 10 mm/h showed more promising structural and morphological properties. The dielectric characterization revealed that all samples have at least one dielectric relaxation phenomenon that is thermally activated. It was also verified that the dielectric constant is higher at a growth pull rate speed of 10 mm/h.

Keywords: $BiFeO_3$; multiferroic; LFZ; dielectric constant; relaxation process

Citation: Peixoto, M.V.; Costa, F.M.; Devesa, S.; Graça, M.P.F. Structural, Morphological and Dielectric Characterization of $BiFeO_3$ Fibers Grown by the LFZ Technique. *Crystals* **2023**, *13*, 960. https://doi.org/10.3390/cryst13060960

Academic Editor: Claudio Cazorla

Received: 29 May 2023
Revised: 11 June 2023
Accepted: 13 June 2023
Published: 16 June 2023

1. Introduction

Multiferroic materials are a special class of solid-state compounds in which two or all three of the ferroic properties, ferroelectricity, ferromagnetism, and ferroelasticity, coexist [1,2]. These materials are considered scientifically and technologically fascinating, not only for their ability to display multiple order states but also for the cross-coupling effects that can occur between the order states [2]. Moreover, there are only a few materials that have two or more ferroic properties; therefore, multiferroic materials are rare [3]. The scarce existence of multiferroics and their potential applications in small, multifunctional, low-power consumption, and environmentally friendly devices make this field of research challenging and justifies the attention given to its development [4,5].

Bismuth ferrite, $BiFeO_3$, has a perovskite structure and is one of the rare multiferroics in which ferroelectricity and magnetism coexist at room temperature. $BiFeO_3$ has a ferroelectric phase transition Curie temperature, T_C, of 1103 K and a G-type antiferromagnetic phase transition Neel temperature, T_N, of 643 K. Due to the high T_C and T_N, well above room temperature, $BiFeO_3$ is considered the most promising and widely known multiferroic material [4–6].

Since it was first synthesized in 1957, $BiFeO_3$ has become one of the most studied multiferroic ceramic materials. However, it is still challenging to synthesize a single-phase $BiFeO_3$ ceramic, with the authors suggesting different reasons for the appearance of the secondary phases [5,7]. They describe $BiFeO_3$ as being metastable, off-stoichiometric, having a low peritectic decomposition temperature, or having its formation affected by Bi_2O_3 evaporation [8–10].

To successfully synthesize single-phase $BiFeO_3$, extensive variation in preparation methods and sintering conditions (temperature, time, and atmosphere) has been applied [7]. $BiFeO_3$ ceramics fabricated by the conventional solid-state reaction have been reported to show a leaky polarization–electric field (P–E) loop or a very low polarization value due to the formation of secondary phases and ionic defects. The single-phase $BiFeO_3$ ceramic,

produced by wet chemical processes such as sol–gel, co-precipitation, and hydrothermal methods, has shown high dielectric losses, low resistivity, or a leaky P–E hysteresis loop [10].

The main objective of this work is the processing and characterization of $BiFeO_3$ fibers. These fibers were obtained by the Laser Floating Zone (LFZ) technique, exploring different growth speeds in order to decrease the secondary phases.

The LFZ technique is a well-known method that enables the production of high-quality crystalline materials in a simple, fast, and crucible-free manner with low consumption of precursor materials [11].

2. Materials and Methods

2.1. Fiber Fabrication

The $BiFeO_3$ fibers were grown by the LFZ technique, using rod precursors for both feed and seed materials prepared by cold extrusion. These rods were obtained by mixing the base powders with polyvinyl alcohol (0.1 g/mL, Merck, Rahway, NJ, USA) to obtain a slurry that was further extruded into cylindrical rods with diameters of 1.75 mm. These rods were allowed to dry in an oven at 50 °C for 1 day. The base powders were prepared by a solid-state reaction using high-purity Bi_2O_3 (Aldrich, St. Louis, MO, USA) and Fe_2O_3 (Merck) as precursors. Stoichiometric amounts of the powders were mixed in a planetary ball system (Pulverisette 7—Fritsch, Idar-Oberstein, Germany), using an agate vessel of 80 mL and agate balls with a total volume of 5.400 cm^3, in a two-cycle process of 60 min at 350 rpm.

The LFZ equipment comprises a 200 W CO_2 laser (Spectron—λ = 10.6 μm) coupled to a reflective optical setup producing a circular crown-shaped laser beam in order to obtain a floating zone configuration with uniform radial heating. Fibers with diameters in the range of 1.5–2 mm and 20–30 mm in length were grown at 5, 10, 25, 50, 100, and 200 mm/h in air at atmospheric pressure.

An advantage of this technique is the possibility of growing materials with preferential alignment of crystals at relatively high speeds, since one of its characteristics is that the temperature gradient in the melt zone is more accentuated than any other technique. On the other hand, if the power of the laser beam is excessive, there may be an excess of liquid in the molten zone. As a result, the growth stops being uniform, the surface tension is altered, and there may be an interruption of the growth process in the liquid/solid zone. Evaporation of some components can also occur due to the fact that the laser power is fully directed to a small region [12].

2.2. Structural, Morphological, and Electrical Measurements

The structural characterization was performed using X-ray diffraction (XRD). The pattern data were obtained on a PANalytical X'Pert PRO diffractometer (CuK α radiation, in the 2θ angle range of 10–60°. Comparing the interplanar distance, d_{hkl}, and the intensities of the reflections with the data catalogued in the JCPDS (Joint Committee on Powder Diffraction Standards) database, it was possible to identify the crystalline phases present in the samples.

For Raman spectroscopy, the Jobin Yvon—Horiba HR 8000 UV spectrometer was used, coupled to a laser with a 532 nm excitation beam and an objective of 50×.

Fiber microstructure and phase development were characterized by scanning electron microscopy (SEM), using a VEGA 3 TESCAN microscope, and by energy dispersive spectroscopy (EDS), using a BRUCKER detector, on polished surfaces of transversal and longitudinal fiber sections.

For the dielectric characterization, the fibers were polished up to a maximum thickness of 0.5 mm. The electrodes were made by covering the opposite sides of the samples with silver conductive paste. This analysis was made in the temperature range of 100 and 380 K, using a nitrogen bath cryostat setup. During the measurements, the samples were kept in a helium atmosphere to avoid moisture and minimize thermal gradients [13–15]. The measurements were made with a Network Analyzer, Agilent 4294, operating between

100 Hz and 1 MHz in the C_p-R_p configuration (capacitance in parallel with resistance). The temperature of the samples was controlled by an Oxford Research IT-C4.

The real and complex parts of the permittivity were calculated using the relations (1) and (2). [16]:

$$\varepsilon' = \frac{d}{S}\frac{C_p}{\varepsilon_0} \tag{1}$$

$$\varepsilon'' = \frac{d}{S}\frac{1}{\omega R_p \varepsilon_0} \tag{2}$$

where C_p is the measured capacitance, R_p is the resistance, ω is the angular frequency, d is the sample thickness, S is the electrode area, and ε_0 is the vacuum permittivity (8.8542×10^{-12} F/m).

In 1972, Macedo et al. [17] presented the complex modulus representation $M^*(\omega)$, which is defined as the inverse of the complex permittivity ($M^* = 1/\varepsilon^*$). In general, for a pure conduction process, a relaxation peak would be observed in the frequency spectra of the imaginary component M'' and no peak would arise in the corresponding plot of ε''. Though, for a dielectric relaxation process, a relaxation peak appears in both the M^* and ε^* representations. Comparisons of the ε^* and M* representations have been used to distinguish localized dielectric relaxation processes from long-range conductivity. Macedo et al. introduced this formalism to study space charge relaxation phenomena; however, the M^* formalism is now widely used to analyze ionic conductivities and is useful to understand the bulk responses of materials, as electrode polarization effects are minimized and the effect of conductivity can be highly suppressed [18].

Physically, the electric modulus corresponds to the relaxation of the electric field in the material when the electric displacement remains constant, so the electric modulus represents the real dielectric relaxation process [19].

The complex modulus can be quantified using the following formula [18]:

$$M^* = M' + jM'' \tag{3}$$

where M' and M'' are the real and imaginary components of the complex modulus, respectively.

The activation energy, E_a, can be evaluated by plotting the frequency corresponding to M'' maximum against reciprocal temperature and fitting the data to the Arrhenius law [20]:

$$f_m = f_0 exp\left(-\frac{E_a}{k_B T}\right) \tag{4}$$

where f_m is the frequency at the relaxation peak, f_0 is a pre-exponential factor, E_a is the activation energy, k_B is the Boltzmann constant, and T is the absolute temperature.

3. Results

Figure 1 depicts the room temperature XRD fiber patterns grown by the LFZ technique with a different growth rate, and the results show that all samples have three crystalline phases: $BiFeO_3$, $Bi_{25}FeO_{40}$, and Fe_2O_3.

Due to the multiphase nature of the fibers grown by LFZ, several fibers were processed with a wide range of growth rates, from 5 mm/h up to 200 mm/h, in order to reduce secondary phases, in particular the $Bi_{25}FeO_{40}$ phase, and thereby increase the amount of the desired phase, the $BiFeO_3$. However, the analysis of the relative intensity of the diffraction peaks shows that the relative amount of each phase is almost constant for the fibers grown at a speed superior to 10 mm/h.

To substantiate this interpretation, the chemical composition of the prepared samples was estimated by Rietveld's refinement method using Profex [21]. Figure 2a shows the measured and calculated spectra for the sample grown at 10 mm/h, and Figure 2b presents the evolution of the percentage, in volume, of the identified phases with the increase in the growth speed.

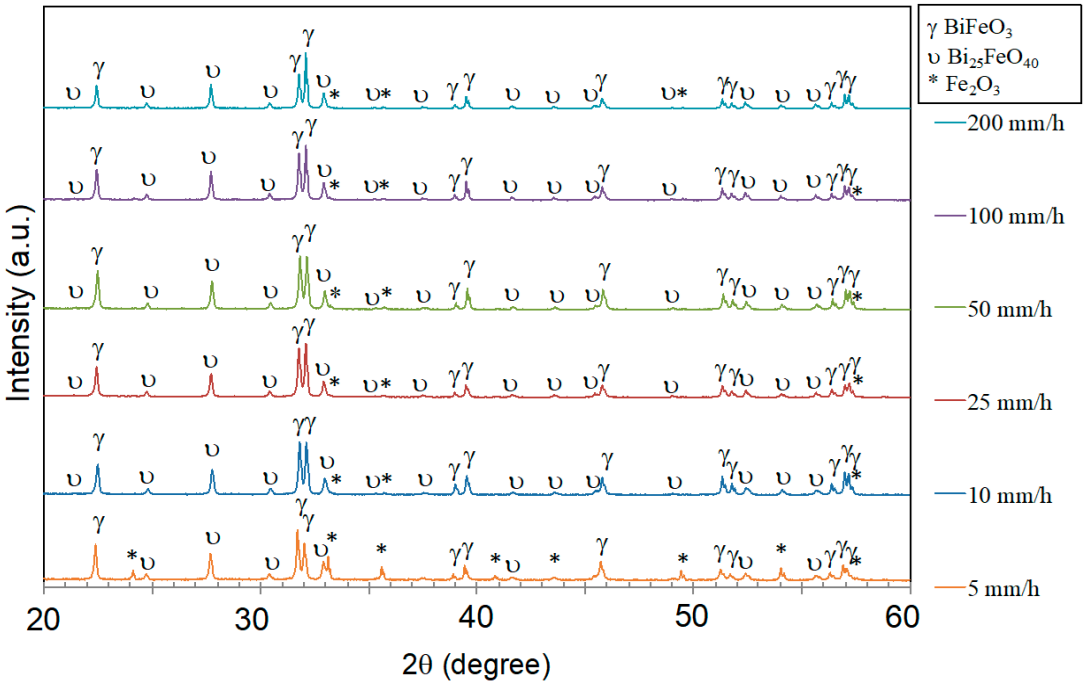

Figure 1. Diffractogram of the prepared fibers and respective indexing.

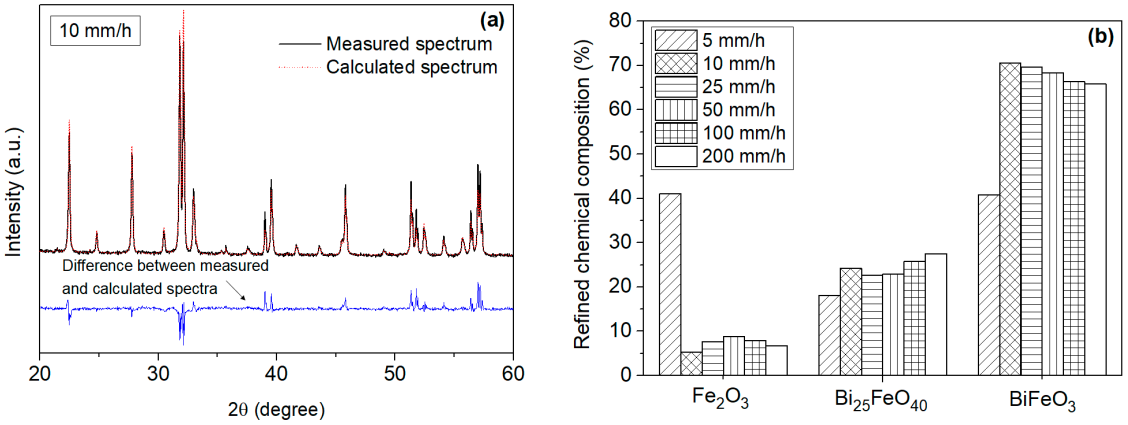

Figure 2. (**a**) Measured and calculated spectra of the fiber grown at 10 mm/h; (**b**) variation, in percentage, of the chemical composition of the prepared samples.

The Rietveld fitting parameters, presented in Table 1, show the good quality of the fitting [22,23] and the consistency of the presented results.

Table 1. Rietveld fitting parameters.

	5 mm/h	10 mm/h	25 mm/h	50 mm/h	100 mm/h	200 mm/h
R_{wp}	4.88	6.88	4.91	5.84	4.70	4.90
R_{exp}	3.08	2.85	2.27	3.29	3.09	3.03
χ^2	2.51	5.83	4.68	3.15	2.31	2.62

The results further show that these $BiFeO_3$ fibers are always the main phase, with $Bi_{25}FeO_{40}$ and Fe_2O_3 as secondary phases. However, despite the growth speed of 5 mm/h allowing the reduction in $Bi_{25}FeO_{40}$ content, there was an increase in the Fe_2O_3 phase. Thus, this sample has the same crystal phases as the remaining fibers, with $Bi_{25}FeO_{40}$ being a minority.

Due to these results, the fibers grown at slower pull rates, 5, 10, and 25 mm/h, were studied in more detail since they presented a more marked change in the relative amount of the identified crystallographic phases, with the fibers grown at 50, 100, and 200 mm/h showing a composition very similar to the 25 mm/h fiber.

To complement the structural characterization of the selected fibers, their transverse and longitudinal sections were analyzed by Raman spectroscopy. Figure 3a shows the Raman spectra of the transverse cross-section of the fibers grown at 5, 10, and 25 mm/h, since the samples grown at 50, 100, and 200 mm/h are, according to the XRD results, very similar to the one grown at 25 mm/h.

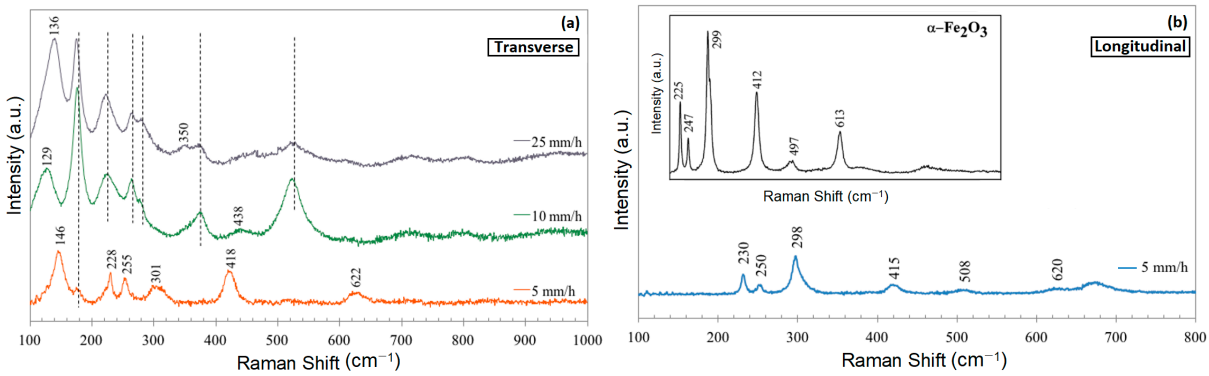

Figure 3. (**a**) Raman spectra of the transverse cross-section of the fibers grown at 5 mm/h, 10 mm/h, and 25 mm/h; (**b**) Raman spectrum of the longitudinal cross-section of the fiber grown at 5 mm/h (inset: Raman spectrum of Fe_2O_3, adapted from [24]).

The location of the peaks in the fibers grown at 25 and 10 mm/h is analogous; however, narrower and more intense bands are observable in the 10 mm/h fiber. This result is consistent with what would be expected since the fibers grown at 10 mm/h are more crystalline because the solidification process was slower. In the fiber grown at 5 mm/h, there is not only a decrease in the intensity and an increase in the half width of the peaks that are shared with the previously analyzed fibers, but also the absence of some peaks, namely the ones centered at 371 and 523 cm^{-1}, and the presence of new peaks, like the ones at 301 and 622 cm^{-1}.

Figure 3b shows the spectrum performed on the longitudinal cross-section of the 5 mm/h fiber. The comparison of these results with the Raman spectrum of Fe_2O_3 [24] shows that this phase is predominant in this fiber, corroborating the XRD data.

According to the literature, the rhombohedral structure R3c of $BiFeO_3$ gives rise to thirteen Raman active modes: four A_1 and nine E [25]. In Table 1, the Raman shifts experimentally obtained for the selected fibers are featured. In accordance with the group theory, of these thirteen modes, four belong to the A_1 modes (136, 174, 224, and 418 cm^{-1}) and nine correspond to the E modes (129, 260, 278, 301, 350, 371, 438, 523, and 622 cm^{-1}). Table 2 also shows the results obtained by Rao et al. [25].

Parejón et al. [26] analyzed nanoparticles of pure $BiFeO_3$, prepared by a mechanochemical process, and identified three bands belonging to the A_1 modes (170, 225, and 415 cm^{-1}) and seven bands corresponding to the E modes (263, 293, 355, 372, 472, 525, and 618 cm^{-1}). Yuan et al. [27] observed eleven modes in Raman $BiFeO_3$ films prepared by a rapid liquid-phase sintering method, consisting of four A_1 modes (126, 166, 213, and 425 cm^{-1}) and six E modes (112, 260, 340, 367, 477, 531, and 600 cm^{-1}). In the fibers of the presented work, there is a band at 129 cm^{-1}, which is confirmed by Rao et al. [25] as belonging to the active mode E_1 for polycrystalline $BiFeO_3$ synthesized by the solid-state reaction method. The slight difference in some of the positions of the bands observed by different researchers can be attributed to the sample preparation method and form.

Table 2. Identification of the Raman modes assigned to the $BiFeO_3$ phase.

Vibrational Modes	25 mm/h (cm^{-1})	10 mm/h (cm^{-1})	5 mm/h (cm^{-1})	Rao et al. [22] (cm^{-1})
E	-	129	-	129
A_1-1	136	-	146	139
A_1-2	174	173	173	172
A_1-3	224	220	228	231
E	264	260	255	261
E	278	278	-	276
E	-	-	301	303
E	350	-	-	346
E	371	372	-	369
A_1-4	-	-	418	432
E	-	438	-	480
E	523	523	-	524
E	-	-	622	-

The comparison of the published values with the experimental results shows that practically all the active modes are present in the fibers grown by LFZ at 25 and 10 mm/h. Among the nine E modes, the mode at ~278 cm^{-1} is associated with covalent bonds Bi-O, which are the cause of ferroelectric distortion. The Bi atoms actively participate in the lower frequency modes (<167 cm^{-1}), while the Fe atoms are mainly involved in modes between 152 and 261 cm^{-1}, but also contribute to some of the high-frequency modes. Finally, the movement of the oxygen atoms predominates in the modes above 262 cm^{-1} [25–28].

Figure 4 shows typical SEM micrographs of the fibers grown at 5, 10, and 25 mm/h. The images were taken on the longitudinal section of the fibers (Figure 4a,d,g) and in the transverse cross-section (Figure 4b,c,e,f,h,i) obtained after polishing the fibers. The micrographs also show the growth direction of the fibers, which is represented by an arrow placed in the images corresponding to the longitudinal section. The images obtained are consistent with the analyses carried out previously since they reveal a polyphasic character, with $BiFeO_3$ being the major phase (darker phase) and $Bi_{25}FeO_{40}$ being the main secondary phase (lighter phase), for samples 25 and 10 mm/h. This identification was based on the elemental quantification measurements made by EDS and is in accordance with reference [29], since the less refractory phases are the bismuth-richer phases that correspond to the lighter phases in SEM micrographs. In the present study, $Bi_{25}FeO_{40}$ is the less refractory phase.

Analyzing the images of the transverse cross-section of the 25 mm/h and the 10 mm/h fibers, particularly the enlarged images, it is seen that the lighter phase appears mainly in the grain boundaries of the darker phase, allowing a better definition of these borders. These enlarged images show a homogeneous microstructure, characterized by cell morphology, revealing that the $BiFeO_3$ crystals have preferential growth along the fiber axis. However, Figure 4b,e shows that this homogeneity is not extensible to the periphery of the fibers, where a darker area is visible and can be ascribed to the Fe_2O_3 phase. These results are consistent with the literature since the most refractory phase, the bismuth-free phase, would be expected to crystallize preferentially on the edges of the fiber, where the cooling is faster [29].

By decreasing the growth speed to 5 mm/h (Figure 4g–i), the fiber ceases to present crystals with well-defined morphology and is notorious for a certain microstructural disorganization. Measurements of elemental quantification by EDS identified the dark phase as being Fe_2O_3 and the lighter one as $BiFeO_3$. With $Bi_{25}FeO_{40}$ being a minor phase, it was not identifiable in these micrographs. Again, these results are consistent with the characterization techniques mentioned above and confirm the presence of large amounts of Fe_2O_3 in fibers with lower growth speeds. This output is visible in the transverse cross-section of the 5 mm/h fiber and can be the result of some loss of bismuth by volatilization. In fact, with a growth rate that low, the time that the material is fused at elevated temperatures

is too long, which may lead to the volatilization of the bismuth since its melting temperature is extremely low when compared with iron oxide.

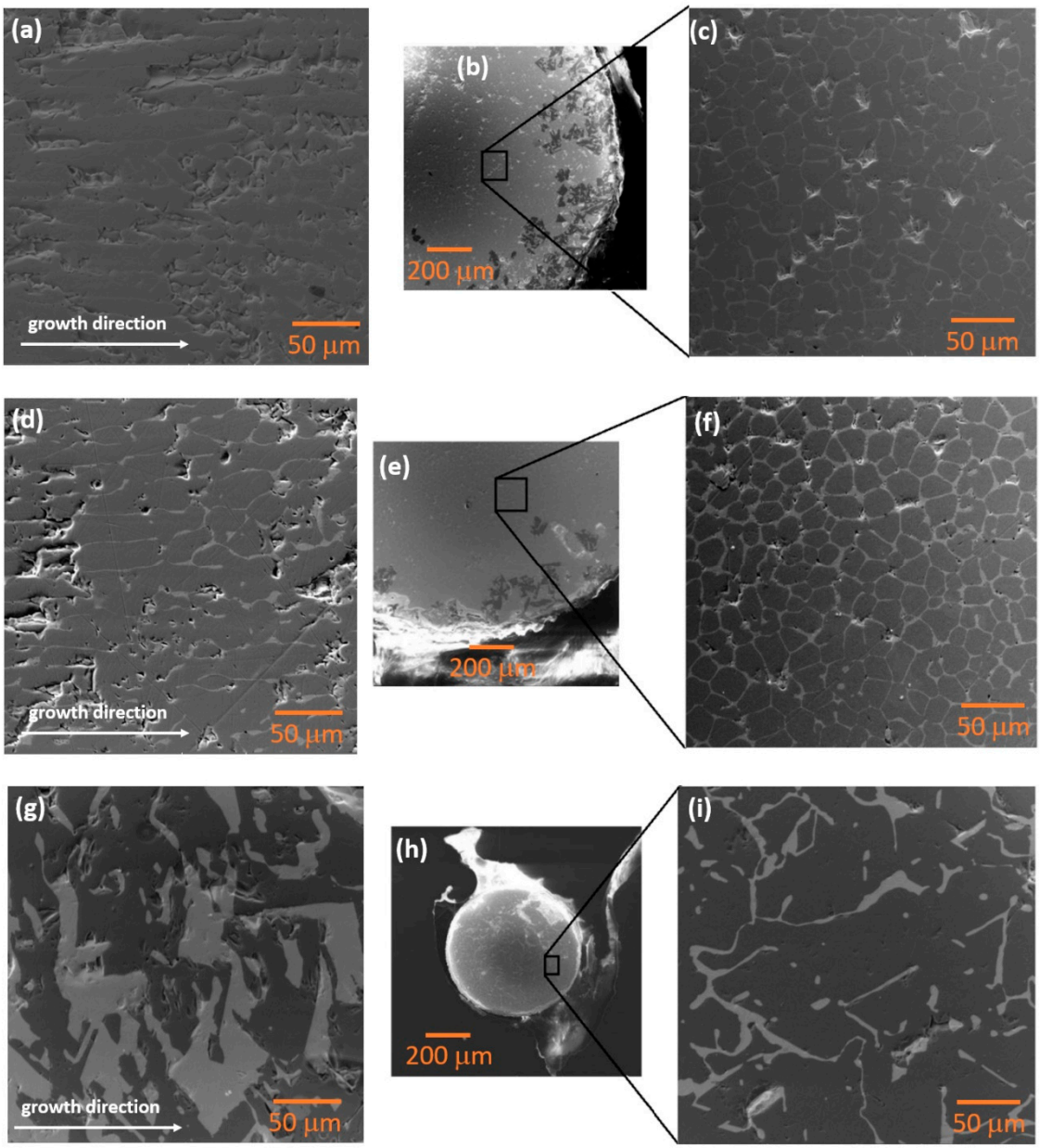

Figure 4. SEM micrographs of the selected fibers: (**a**) longitudinal cross-section of the 25 mm/h fiber; (**b**) transverse cross-section of the 25 mm/h fiber; (**c**) enlarged image of the selected area in (**b**); (**d**) longitudinal cross-section of the 10 mm/h fiber; (**e**) transverse cross-section of the 10 mm/h fiber; (**f**) enlarged image of the selected area in (**e**); (**g**) longitudinal cross-section of the 5 mm/h fiber; (**h**) transverse cross-section of the 5 mm/h fiber; (**i**) enlarged image of the selected area in (**h**).

Figure 5 shows the dielectric constant, ε', as a function of frequency at three different temperatures for the fibers grown at 5, 10, 25, and 200 mm/h. The results show that, in general, ε' increases with the temperature, with the fiber grown at 10 mm/h showing higher dielectric constant values in the frequency range and temperatures analyzed.

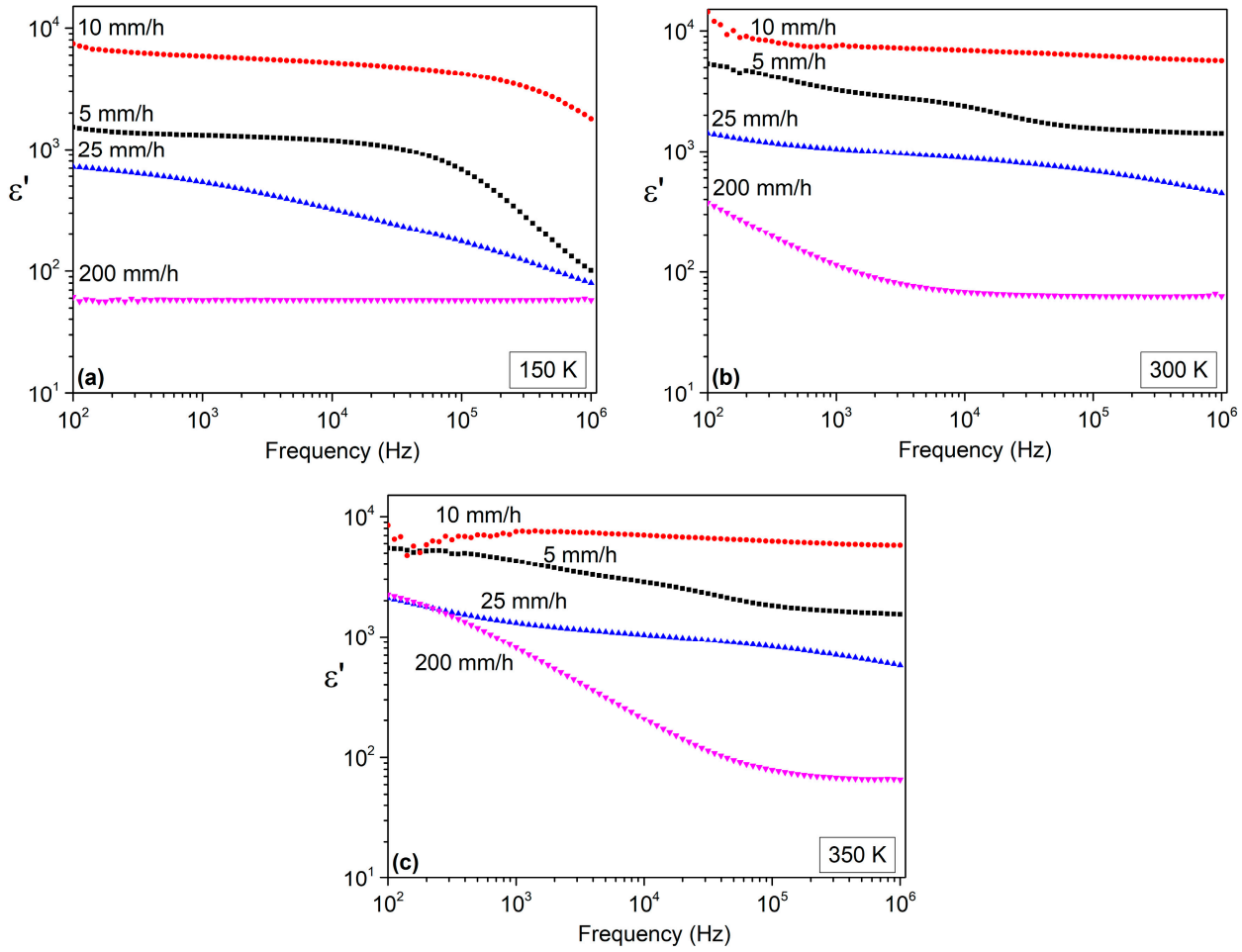

Figure 5. Frequency dependence of the dielectric constant, measured at (**a**) 150 K, (**b**) 300 K, and (**c**) 350 K, for the fibers grown at 5, 10, 25, and 200 mm/h.

According to [30], the ε' of $BiFeO_3$, prepared by the solid-state method, measured at room temperature and at a frequency of 100 kHz, is approximately 80. In the present study, the obtained values are significantly higher, and this difference can be related to the existence of a preferential direction for the $BiFeO_3$ crystals growth (along the fiber axis), thereby maximizing the dielectric response. However, other aspects must be taken into consideration, such as the existence of the secondary phases, $Bi_{25}FeO_{40}$ and Fe_2O_3. Therefore, for the dielectric response, factors such as electrode-sample interfaces and the interfaces between phases must be considered.

Since the amount of Fe_2O_3, which has, at room temperature and at 100 kHz, a dielectric constant of 1.3 [31], is reduced when compared to the $BiFeO_3$ and $Bi_{25}FeO_{40}$ phases, it is reasonable to assume that its contribution to the dielectric response in the sample grown at 10 mm/h is secondary. Moreover, from the morphological analysis, it is suggested that the dipoles formed between the $BiFeO_3$ and $Bi_{25}FeO_{40}$ interfaces, due to their higher amount in this fiber, are the main reason for the high ε' value.

The presence of the $Bi_{25}FeO_{40}$ phase also gives rise to the formation of oxygen gaps and the multiplicity of Fe ions (Fe^{2+} and Fe^{3+}), increasing the conductivity [32]. This increase is clearly visible in the tangent losses depicted in Figure 6, which are the maximum for the sample grown at 10 mm/h.

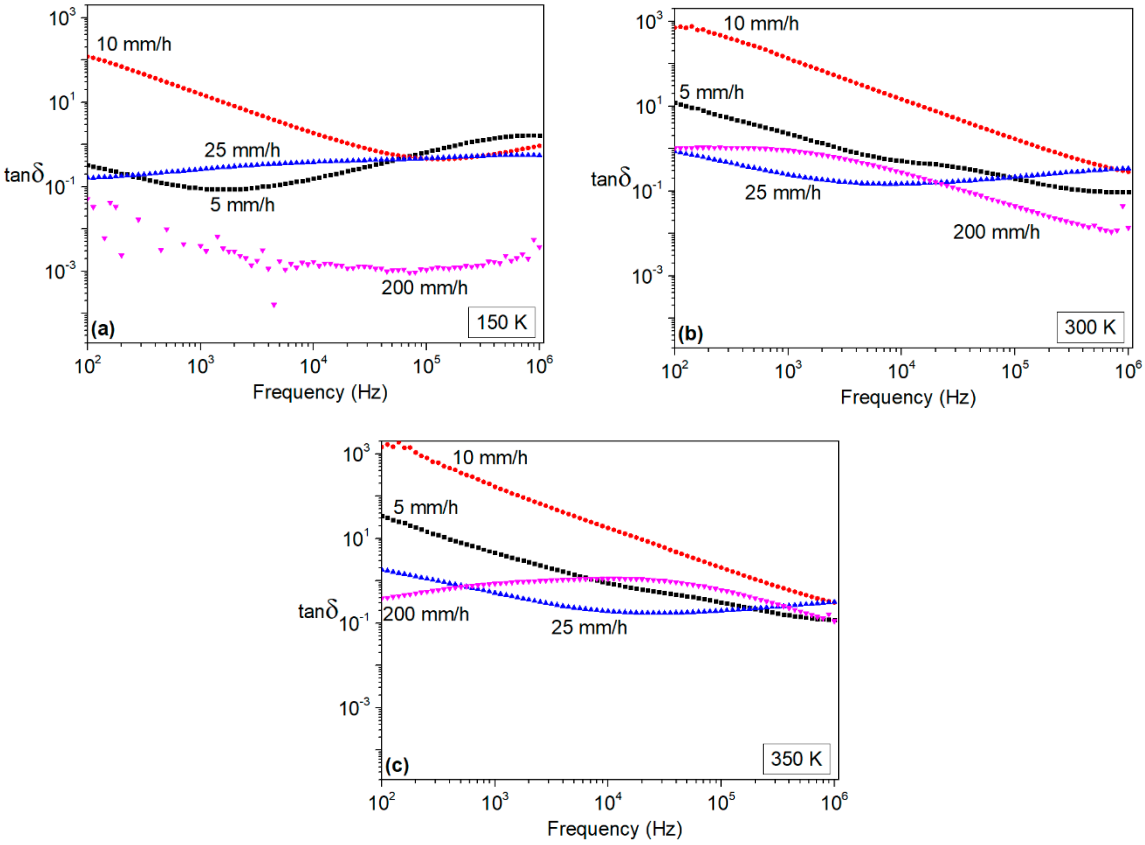

Figure 6. Frequency dependence of the loss tangent, measured at (**a**) 150 K, (**b**) 300 K, and (**c**) 350 K, for the fibers grown at 5, 10, 25, and 200 mm/h.

Plotting the imaginary part of the dielectric modulus, M'', as a function of frequency for all growth speeds, it is observed that dielectric relaxation phenomena exist. In all the samples and in all the observed relaxation processes, the peak shifts to a higher frequency with the increase in temperature, indicating that the response of the dipoles to the external electric field becomes easier at higher temperatures.

Figure 7 shows the variation of the imaginary part of the modulus with frequency for the fibers grown at 5, 10, 25, and 200 mm/h.

It is interesting to note that in the sample at 5 mm/h, where the Fe_2O_3 content is higher, three relaxation processes are visible. The inset of Figure 7a highlights the two relaxation phenomena that occur at higher temperatures. On the other hand, the samples grown at 10 and 25 mm/h, where the chemical content is very similar, show two relaxations in the measurement window. In the 10 mm/h sample, the second relaxation occurs at high temperatures and high frequencies. In the case of the 25 mm/h fiber, the inset of Figure 7c highlights the relaxation visible at low frequencies and high temperatures. Finally, the sample at 200 mm/h, where the $Bi_{25}FeO_{40}$ content is higher, shows a relaxation phenomenon in the measurement window.

By examining the variation in the peak corresponding to M'' maximum as a function of inverse temperature (Figure 8), it appears that this follows the Arrhenius law, Equation (4), allowing the estimation of the activation energy for each relaxation phenomenon.

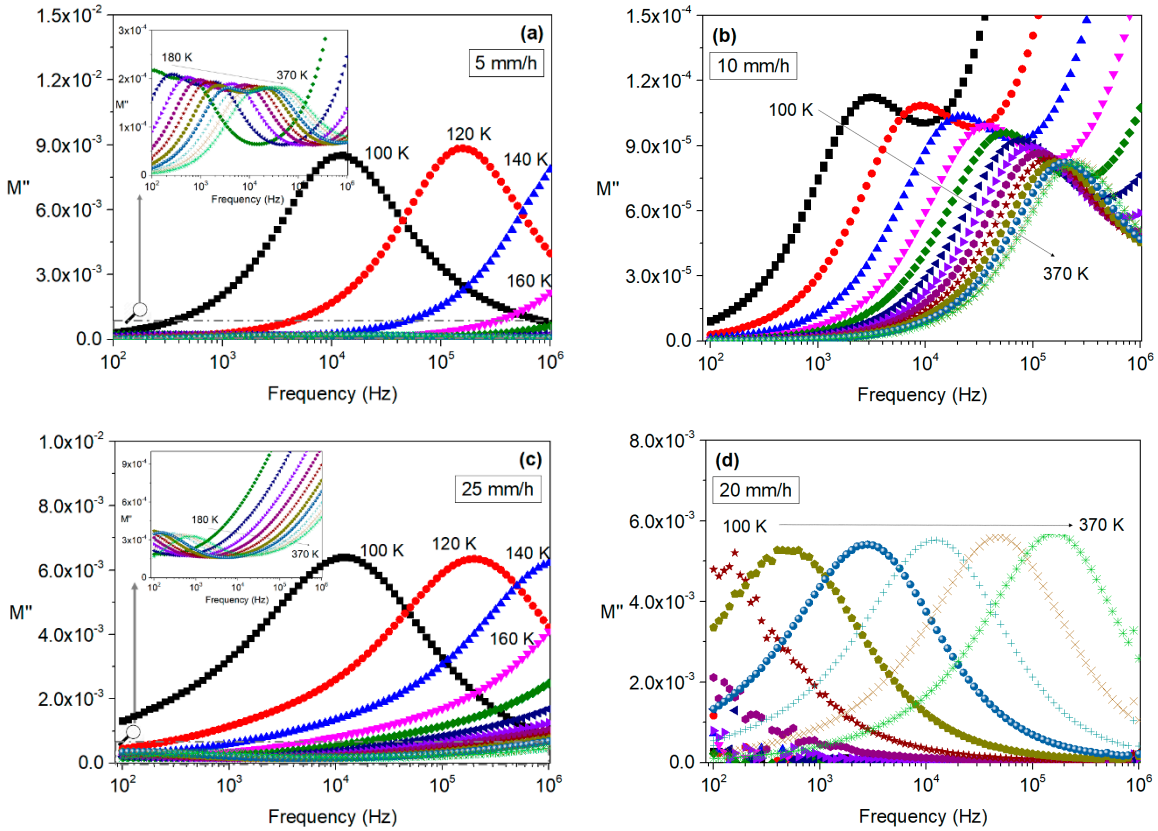

Figure 7. Imaginary part of the modulus, M'', as a function of frequency, for temperatures between 100 and 370 K, in steps of 10 K, for the fibers grown at (**a**) 5 mm/h; (**b**) 10 mm/h; (**c**) 25 mm/h; (**d**) 200 mm/h.

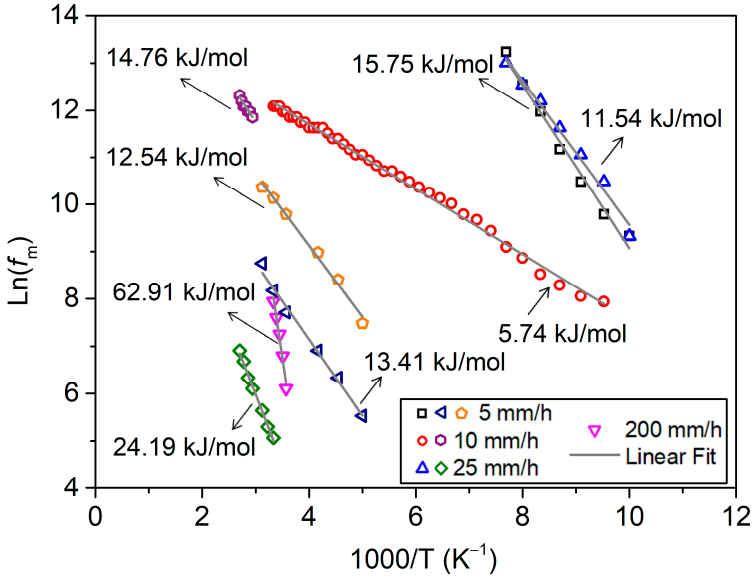

Figure 8. Arrhenius plot of the peak frequencies obtained from the imaginary part of the electrical modulus.

Table 3 shows the activation energy values, distinguishing them according to the frequency region and temperature of occurrence in the case of multiple phenomena.

Table 3. Activation energy values of the relaxation phenomena identified (LT—Low temperature; HT—High temperature; LF—Low frequency; HF—High frequency).

	5 mm/h	10 mm/h	25 mm/h	200 mm/h
Activation energy (kJ/mol)	LT/HF 15.75	LT/LF 5.74	LT/HF 11.54	62.91
	HT/LF 13.41			
	HT/HF 12.54	HT/HF 14.76	HT/LF 24.19	

Despite the similar chemical composition of the fibers grown at 10, 25, and 200 mm/h, the increase in the growth speed is not irrelevant to the values estimated for the activation energy. The lower activation energy for the relaxation mechanisms of the 10 mm/h sample can be related to the higher amount, when compared to the other samples, of interfaces between the $BiFeO_3$ and $Bi_{25}FeO_{40}$.

The activation energies of samples grown at 50 mm/h and 100 mm/h were calculated, showing values similar to the sample activation energy of the 200 mm/h fiber.

4. Conclusions

$BiFeO_3$-based fibers were prepared through the LFZ technique at different growth speeds (5, 10, 25, 50, 100, and 200 mm/h). The XRD results show that all samples are polyphasic, with $BiFeO_3$ always being the main phase. Therefore, the speeds that have been shown to be the most promising were the ones grown at 10 and 25 mm/h. These fibers are very similar; however, there are narrower and more intense bands in the Raman spectrum of the 10 mm/h fiber and a higher content of the $BiFeO_3$ phase, as confirmed by the Rietveld analysis. The fiber grown at 5 mm/h reveals a differentiated behavior due to the higher content of the Fe_2O_3 phase.

The images obtained by scanning electron microscopy are consistent with the structural analyses since they show a polyphasic character. Comparing the image of the transversal cross-section of the 25 mm/h fiber with the one grown at 10 mm/h, it can be seen that the $Bi_{25}FeO_{40}$ phase appears mainly in the grain boundaries, allowing a greater definition of these boundaries. Decreasing the growth speed to 5 mm/h, the $BiFeO_3$ phase ceases to present crystals with a well-defined morphology, and there is a noticeable microstructural disorganization. Additionally, in this sample, $Bi_{25}FeO_{40}$ was not visible since it is a minor phase.

The results of the dielectric analysis show that the fiber with a higher content of $BiFeO_3$, the 10 mm/h sample, showed a higher dielectric constant, regardless of temperature and frequency. The loss tangent was also higher for this sample. For all growth velocities, the existence of multiple dielectric relaxation phenomena was observed. The fibers grown at 10 and 25 mm/h showed two relaxations, with the activation energy increasing with the increase in temperature for which the phenomenon was observable. This analogous behavior was expected due to the structural and morphological similarity. The sample grown at 5 mm/h showed an extra relaxation process that can be attributed to the higher content of Fe_2O_3 when compared to the remaining samples. Contrary, the sample grown at 200 mm/h presented one relaxation phenomenon in the measurement window, with activation energy considerably higher. This different behavior can be attributed to the higher content of the $Bi_{25}FeO_{40}$ phase.

Author Contributions: Conceptualization, M.P.F.G. and F.M.C.; methodology, M.V.P., F.M.C., M.P.F.G.; software, M.V.P. and S.D.; validation, F.M.C. and M.P.F.G.; formal analysis, F.M.C., S.D. and M.P.F.G.; investigation, M.V.P., F.M.C. and M.P.F.G.; resources, M.P.F.G. and F.M.C.; data curation, M.V.P.; writing—original draft preparation, M.V.P.; writing—review and editing, M.P.F.G., F.M.C. and S.D.;

visualization, M.V.P. and S.D.; supervision, M.P.F.G. and F.M.C.; project administration, M.P.F.G.; funding acquisition, M.P.F.G. All authors have read and agreed to the published version of the manuscript.

Funding: This research was funded by FEDER funds through the COMPETE 2020 Program and National Funds through FCT—Portuguese Foundation for Science and Technology under the project LISBOA-01-0247-FEDER-039985/POCI-01-0247-FEDER-039985 LA/P/0037/2020, UIDP/50025/2020, and UIDB/50025/2020 of the Associate Laboratory Institute of Nanostructures, Nanomodelling, and Nanofabrication—i3N.

Data Availability Statement: The raw/processed data required to reproduce these findings cannot be shared at this time, as the data also form part of an ongoing study.

Conflicts of Interest: The authors declare no conflict of interest.

References

1. Martin, L.W.; Crane, S.P.; Chu, Y.H.; Holcomb, M.B.; Gajek, M.; Huijben, M.; Yang, C.H.; Balke, N.; Ramesh, R. Multiferroics and magnetoelectrics: Thin films and nanostructures. *J. Phys. Condens. Matter* **2008**, *20*, 434220. [CrossRef]
2. Vopson, M. Fundamentals of Multiferroic Materials and Their Possible Applications. *Crit. Rev. Solid State Mater. Sci.* **2015**, *40*, 223. [CrossRef]
3. Khomskii, D. Classifying multiferroics: Mechanisms and effects. *Physics* **2009**, *2*, 20. [CrossRef]
4. Lone, I.H.; Aslam, J.; Radwan, N.R.E.; Bashal, A.H.; Ajlouni, A.F.A.; Akhter, A. Multiferroic ABO_3 Transition Metal Oxides: A Rare Interaction of Ferroelectricity and Magnetism. *Nanoscale Res. Lett.* **2019**, *14*, 142. [CrossRef] [PubMed]
5. Wang, N.; Luo, X.; Han, L.; Zhang, Z.; Zhang, R.; Olin, H.; Yang, Y. Structure, Performance, and Application of $BiFeO_3$ Nanomaterials. *Nano-Micro Lett.* **2020**, *12*, 81. [CrossRef] [PubMed]
6. Yang, C.H.; Kan, D.; Takeuchi, I.; Nagarajan, V.; Seidel, J. Doping $BiFeO_3$: Approaches and enhanced functionality. *Phys. Chem. Chem. Phys.* **2012**, *14*, 15953–15962. [CrossRef] [PubMed]
7. Valant, M.; Axelsson, A.; Alford, N. Peculiarities of a solid-state synthesis of multiferroic polycrystalline $BiFeO_3$. *Chem. Mater.* **2007**, *19*, 5431–5436. [CrossRef]
8. Levin, E.M.; Roth, R.S. Polymorphism of bismuth sesquioxide. II. Effect of oxide additions on the polymorphism of Bi_2O_3. *J. Res. Natl. Bur. Stand.* **1964**, *68*, 197. [CrossRef]
9. Morozov, M.; Lomanova, N.A.; Gusarov, V.V. Specific Features of $BiFeO_3$ Formation in a Mixture of Bismuth(III) and Iron(III) Oxides. *Russ. J. Gen. Chem.* **2003**, *73*, 1676–1680. [CrossRef]
10. Kim, A.Y.; Lee, Y.J.; Kim, J.S.; Han, S.H.; Kang, H.W.; Lee, H.G.; Cheon, C.I. Ferroelectric properties of $BiFeO_3$ ceramics sintered under low oxygen partial pressure. *J. Korean Phys. Soc.* **2012**, *60*, 83–87. [CrossRef]
11. Rey-García, F.; Ibáñez, R.; Angurel, L.A.; Costa, F.M.; de la Fuente, G.F. Laser Floating Zone Growth: Overview, Singular Materials, Broad Applications, and Future Perspectives. *Crystals* **2021**, *11*, 38. [CrossRef]
12. Ritzert, F.; Westfall, L. *Laser-Heated Floating Zone Production of Single-Crystal Fibers, NASA Technical Memorandum 4732*; Lewis Research Center: Cleveland, OH, USA, 1996. Available online: https://ntrs.nasa.gov/citations/19960017267 (accessed on 10 May 2023).
13. Devesa, S.; Graça, M.P.; Costa, L.C. Impedance Spectroscopy Characterization of a Niobate Material for RF Applications. In *Advances in Chemistry Research*; Taylor, J.C., Ed.; Nova Science Publishers: Hauppauge, NY, USA, 2022; Volume 76, pp. 175–205. [CrossRef]
14. Graça, M.P.F.; da Silva, M.F.; Valente, M.A. $NaNbO_3$ crystals dispersed in a B_2O_3 glass matrix–Structural characteristics versus electrical and dielectrical properties. *Solid State Sci.* **2009**, *11*, 570–577. [CrossRef]
15. Graça, M.P.F.; da Silva, M.F.; Sombra, A.S.B.; Valente, M.A. Electric and dielectric properties of a SiO_2–Na_2O–Nb_2O_5 glass subject to a controlled heat-treatment process. *Phys. B* **2007**, *396*, 62–69. [CrossRef]
16. Devesa, S.; Graça, M.P.; Costa, L.C. Impedance Spectroscopy Study of $Bi_{1.34}Fe_{0.66}Nb_{1.34}O_{6.35}$ Ceramics. *J. Electron. Mater.* **2021**, *50*, 4135–4144. [CrossRef]
17. Macedo, P.B.; Moynihan, C.T.; Bose, R. The Role of Ionic Diffusion in Polarization in Vitreous Ionic. *Phys. Chem. Glas.* **1972**, *13*, 171–179.
18. Zaman, A.; Uddin, S.; Mehboob, N.; Tirth, V.; Algahtani, A.; Abbas, M.; Mushtaq, M.; Ali, A.; Sultana, F.; Althubeiti, K.; et al. Structural Elucidation, Electronic and Microwave Dielectric Properties of $Ca(Sn_xTi_{1-x})O_3$, ($0 \leq x \leq 0.8$) Lead-Free Ceramics. *ACS Omega* **2022**, *7*, 4667–4676. [CrossRef] [PubMed]
19. Liu, J.; Duan, C.G.; Yin, W.G.; Mei, W.N.; Smith, R.W.; Hardy, J.R. Dielectric permittivity and electric modulus in $Bi_2Ti_4O_{11}$. *J. Chem. Phys.* **2003**, *119*, 2812. [CrossRef]
20. Raja, V.; Sharma, A.K.; Rao, V.V.R.N. Impedance spectroscopic and dielectric analysis of PMMA-CO-P4VPNO polymer films. *Mater. Lett.* **2004**, *58*, 3242–3247. [CrossRef]
21. Doebelin, N.; Kleeberg, R. Profex: A graphical user interface for the Rietveld refinement program BGMN. *J. Appl. Cryst.* **2015**, *48*, 1573–1580. [CrossRef]
22. Toby, B.H. R factors in Rietveld analysis: How good is good enough? *Powder Diffr.* **2006**, *21*, 67–70. [CrossRef]

23. Devesa, S.; Rooney, A.P.; Graça, M.P.; Cooper, D.; Costa, L.C. Williamson-hall analysis in estimation of crystallite size and lattice strain in $Bi_{1.34}Fe_{0.66}Nb_{1.34}O_{6.35}$ prepared by the sol-gel method. *Mater. Sci. Eng. B* **2021**, *263*, 114830. [CrossRef]
24. Lu, J.F.; Tsai, C.J. Hydrothermal phase transformation of hematite to magnetite. *Nanoscale Res. Lett.* **2014**, *9*, 230. [CrossRef] [PubMed]
25. Rao, T.D.; Asthana, S.; Niranjan, M.K. Observation of coexistence of ferroelectric and antiferroelectric phases in Sc substituted $BiFeO_3$. *J. Alloys Compd.* **2015**, *642*, 192–199. [CrossRef]
26. Perejón, A.; Murafa, N.; Sánchez-Jiménez, P.E.; Criado, J.M.; Subrt, J.; Dianez, M.J.; Pérez-Maqueda, L.A. Direct mechanosynthesis of pure $BiFeO_3$ perovskite nanoparticles: Reaction mechanism. *J. Mater. Chem. C* **2013**, *1*, 3551–3562. [CrossRef]
27. Yuan, G.L.; Or, S.W.; Chan, H.L.W. Raman scattering spectra and ferroelectric properties of $Bi_{1-x}Nd_xFeO_3$ (x= 0–0.2) multiferroic ceramics. *J. Appl. Phys.* **2007**, *101*, 064101. [CrossRef]
28. Hermet, P.; Goffinet, M.; Kreisel, J.; Ghosez, P. Raman and infrared spectra of multiferroic bismuth ferrite from first principles. *Phys. Rev. B Condens. Matter* **2007**, *75*, 220102. [CrossRef]
29. Costa, F.M.; Ferreira, N.M.; Rasekh, S.; Fernandes, A.J.S.; Torres, M.A.; Madre, M.A.; Diez, J.C.; Sotelo, A. Very large superconducting currents induced by growth tailoring. *Cryst. Growth Des.* **2015**, *15*, 2094–2101. [CrossRef]
30. Yuan, G.L.; Or, S.W.; Chan, H.L.W.; Liu, Z.G. Reduced ferroelectric coercivity in multiferroic $Bi_{0.825}Nd_{0.175}FeO_3$ thin film. *J. Appl. Phys.* **2007**, *101*, 024106. [CrossRef]
31. Kamiyama, S.; Iwaya, M.; Takeuchi, T.; Akasaki, I.; Syväjärvi, M.; Yakimova, R. Fluorescent SiC and its application to white light-emitting diodes. *J. Semicond.* **2011**, *32*, 013004. [CrossRef]
32. Ke, Q.; Lou, X.; Wang, Y.; Wang, J. Oxygen-vacancy-related relaxation and scaling behaviors of $Bi_{0.9}La_{0.1}Fe_{0.98}Mg_{0.02}O_3$ ferroelectric thin films. *Phys. Rev. B Condens. Matter* **2010**, *82*, 024102. [CrossRef]